Nanoscale

ROYAL SOCIETY OF CHEMISTRY

COMMUNICATION

View Article Online
View Journal | View Issue

Cite this: *Nanoscale*, 2024, **16**, 6934

Received 14th January 2024,
Accepted 11th March 2024

DOI: 10.1039/d4nr00195h

rsc.li/nanoscale

Quantifying particle concentration *via* AI-enhanced optical coherence tomography

Siqi Ye, [a] Lei Xing,[a] David Myung[b,c] and Fang Chen *[b]

Efficient and robust quantification of the number of nanoparticles in solution is not only essential but also insufficient in nanotechnology and biomedical research. This paper proposes to use optical coherence tomography (OCT) to quantify the number of gold nanorods, which exemplify the nanoparticles with high light scattering signals. Additionally, we have developed an AI-enhanced OCT image processing to improve the accuracy and robustness of the quantification result.

[a]*Department of Radiation Oncology, Stanford University, Stanford, CA, 94305, USA. E-mail: yesiqi@stanford.edu, lei@stanford.edu*
[b]*Spencer Center for Vision Research, Byers Eye Institute, Department of Ophthalmology, Stanford University School of Medicine, Stanford, CA, 94305, USA. E-mail: david.myung@stanford.edu, fachen@stanford.edu*
[c]*Department of Chemical Engineering, Stanford University, CA, 94305, USA*

Fang Chen

Dr Chen is an instructor in the Department of Ophthalmology at Stanford University. Her research focuses on materials science and engineering approaches to biological or biomedical problems. Specifically, she is dedicated to understanding the design principles and developing nanoscale and macroscale biomaterials for medical applications, experimental investigations of cell therapies, and integration across multiple disciplines including materials science, chemistry, medical imaging, and life science. Her ongoing projects are developing nanoparticles (funded by the NIH K99/R00 award) and hydrogels to treat various eye diseases. Dr Chen has published over 30 peer-reviewed papers and co-authored 4 patents.

1 Introduction

1.1 A demand for particle concentration quantification

In the realm of nanotechnology and biomedical research, the accurate quantification of particle concentration, *i.e.*, the number of nanoparticles in the solution, serves as a fundamental basis for comparing and optimizing the properties of nanoparticles for various applications, such as medical imaging, drug delivery, and nanotechnology research. Gold nanoparticles (GNPs) are biocompatible and have unique physical properties, such as surface plasmon resonance (SPR) and the ability to convert light into heat. They have been broadly used as diagnostic and therapeutic agents. GNPs commonly serve as contrast agents for photoacoustic imaging,[1,2] optical coherence tomography (OCT),[3–6] and computed tomography (CT).[7–9] They are also photothermal therapy or photodynamic therapy agents for cancer treatment.[10–14] Additionally, they can function as drug carriers and enhance the delivery to cells due to their small size and high surface area.[15–17] Precise dosage control of GNPs is crucial for optimizing biomedical applications while minimizing or avoiding side effects. This demands the accurate quantification of the particle concentration. However, the quantification of particle concentration is challenging due to the versatile morphologies and size distributions of GNPs. The development of an efficient and reliable approach to tracking and quantifying GNPs is urgently necessary.

1.2 Nanoparticle concentration quantification techniques

Several methods have been developed to quantify particle concentration. Nanoparticle tracking analysis (NTA) is the only technique to directly quantify the particle concentration of nanoparticles currently.[18–20] This technique utilizes light scattering and Brownian motion analysis to provide information on the particle size and concentration. However, NTA often faces challenges in resolving individual particle populations in samples with diverse size distribution or high polydispersity. The particle size by NTA is an average hydrodynamic diameter, which is hardly the true dimension of either isotropic or anisotropic

nanoparticles. It may also lead to inaccurate quantification when particle motions deviate from the assumed Brownian motion, such as the settling motion of large aggregates. A multi-spectral advanced nanoparticle tracking analysis (MANTA) has been invented to improve the characterization of polydisperse nanoparticles.[21] Nevertheless, NTA is mainly used for liposomes, exosomes, and polymeric nanoparticles. Its quantification for other nanoparticles still demands standardization.

Another typical quantification technique is electron microscopy (EM).[22–24] The EM offers high-resolution visualization of particles at the nanometer scale. It is capable of measuring the size distribution of GNPs and revealing the sizes of a small anisotropic nanoparticle. However, EM is a cumbersome technique for particle concentration determination, requiring scanning the entire sample holder after adding a particle solution of known volume onto it. Moreover, particle stacking will cause inaccurate quantification. The morphology and size measured by EM, however, can be used to determine the volume of individual nanoparticles. This volume could be used to calculate the theoretical particle concentration when the density and mass concentration are known. The mass concentration of gold nanoparticles can be accurately measured by inductively coupled plasma-mass spectrometry (ICP-MS).[25] The theoretical particle concentration will be the total volume of nanoparticles (the mass concentration divided by the density of gold) divided by the volume of a single nanoparticle. This theoretical particle concentration is more accurate for a monodispersed sample than samples with a broad size distribution. Of note, this calculation ignores the effect of aggregation on the actual particle concentration.

While nanoparticles have been widely investigated as contrast agents to improve biomedical imaging, here we propose to use biomedical imaging to characterize nanoparticles. Specifically, we demonstrate the quantification of gold nanorods (GNRs) based on their OCT signals.[4–6,26,27] OCT utilizes low-coherence interferometry to capture cross-sectional images of tissues, enabling non-invasive and real-time capturing of scanned objects. OCT is considered an optical version of ultrasound imaging, but it has a much higher resolution (subcellular) when compared to ultrasound imaging. This method is efficient and can potentially apply to any nanoparticles with high light scattering properties, which is the source of the OCT signal. Moreover, we developed an artificial intelligence (AI) image enhancement method to improve the OCT images. Our results showed that the OCT-based approach took the effect of aggregation into account and reflected the real particle concentration. With an aggregation correction algorithm and AI enhancement, the resulting OCT-based particle concentration is almost identical to the theoretical particle concentration.

2 Method

2.1 Sample preparation and OCT image acquisition

We conducted nanoparticle counting on GNR solution purchased from NanoComposix (product #: GRCH800). Double-distilled water was used to prepare dilution solutions with factors of 800×, 1600×, 3200×, 6400×, and 12800×. The diluted solutions were then loaded into a glass tube with an inner diameter of 1.1 mm through a capillary effect. Double-distilled water was also loaded as a reference for each scan.

The sample-loaded glass tubes were positioned on a sample holder and scanned with a commercial SD-OCT system (SPECTRALIS®HRA+OCT w/OCT2 MultiColor model, Heidelberg). The OCT captured a sequence of 2D images at a non-perpendicular angle along the longitudinal axis of each tube. Images of samples to be compared were obtained within the same scan. We selected distinct sections from the recorded sequence of images as regions of interest (ROIs), delineating the 3D distribution of the solution within the tube. Fig. 1(a) shows the experimental setup described above. An example of images acquired at a specific ROI is shown in Fig. 1(b). The red box indicates the cropped ROI upon which our subsequent processes were based.

2.2 AI-enhanced imaging module

We developed a super-resolution (SR) technique based on the implicit neural representation (INR)[28] for the AI-enhanced imaging module. As illustrated in Fig. 1(c), the INR network utilizes the spatial coordinates of the high-resolution (HR) image as inputs and generates the expected HR image as output. The INR network consists of a Fourier feature embedding block and a multilayer perceptron, aiming to map low-variational coordinate data to high-variational image intensity values. To train the INR network, we converted the network output into the low-resolution (LR) image domain and compared it to the acquired LR image. The SR process involved the use of a classical degradation model that includes image blurring and downsampling for the HR-to-LR image conversion. No extra data but the acquired LR image is needed in this SR process. This is particularly beneficial for applications such as image-based GNR concentration quantification, where HR images for model training may be lacking.

To improve the efficiency and standardization of the SR process, we cropped a square-shaped region of size 60 × 60 pixels located at the center of each ROI, as shown in Fig. 1(b). We assumed nanoparticles were uniformly distributed within the cropped ROI, representing the distribution of nanoparticles in the specific cross-section of the tube. The resolu-

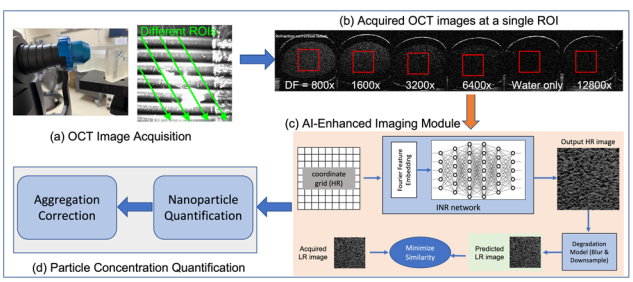

Fig. 1 AI-enhanced OCT imaging for nanoparticle quantification.

tion of the cropped ROI was enhanced by two times, resulting in an image containing 120 × 120 pixels for the subsequent quantification process.

2.3 Quantification and aggregation correction

We used the ImageJ software[29] to analyze the original and AI-enhanced OCT images for nanoparticle quantification, involving two steps: (1) nanoparticle detection and (2) nanoparticle counting. An OCT image contains both dilution solvent and nanoparticles. In the detection step, we applied a threshold to filter out background pixels. Using the double-distilled water as a reference, we found the maximum lower threshold when the nanoparticle number is zero in the water. After thresholding, the particle analysis tool in ImageJ was employed to detect nanoparticles. The count of detected image patches, exemplified by the rectangular-shaped small portion within the zoom-in box in Fig. 2, was regarded as the number of nanoparticles in the OCT image.

We also introduced an aggregation correction step to address the nanoparticle aggregation effect. The aggregation correction was based on the area of the detected nanoparticles. We assumed that each nanoparticle occupies only 1-pixel^2 area on the original OCT image, and it occupies 4-pixel^2 area on the AI-enhanced images with 2× resolution enhancement. This assumption is reasonable for any morphologies of the gold nanoparticles because the length of the long-axis of a gold nanoparticle usually ranges from 10–200 nm,[30] which is significantly smaller than the approximate distance of several centimeters between the source of the reflected light to the detector.

3 Results and discussion

We evaluated the quantification results from three perspectives and found that AI-enhanced OCT imaging improved the particle concentration quantification. First, the AI-enhanced OCT imaging improved the linear fitting of particle concentrations and the dilution factors (*i.e.*, theoretical concentrations). Second, quantification based on AI-enhanced OCT images provided almost identical particle concentration to the theoretical concentration, which is much more accurate compared with using no AI-involved original OCT images. Third, the slope of the regression line of the experimental and theoretical particle concentrations should be close to 1, indicating the two concentrations are identical with different dilution factors. Only the aggregation-corrected particle concentrations resulting from the AI-enhanced OCT images showed such a slope in the regression analysis. As a comparison baseline, we performed image enhancement *via* a conventional interpolation method. Analysis based on the interpolated OCT images yielded similar results to those obtained using the original OCT images.

The mass concentration of gold in the GNRs was found to be 0.92 mg mL^{-1} measured by ICP-MS. The average diameter and length of the GNRs were measured to be 18.0 nm and 74.6 nm respectively according to the transmission electron microscope analysis. The density of a GNR is 19.3 g mL^{-1}. The theoretical concentration of the GNRs was calculated to be 2.51×10^{12} particles per mL, using the equation:

$$[\mathrm{GNR}](\text{particles per mL}) = \frac{\text{mass concentration of Au in the GNR suspension}}{(\text{density of Au}) \times (\text{volume of a single GNR})}.$$

The theoretical particle concentrations of the 800×, 1600×, 3200×, 6400×, and 12 800× diluted GNR solutions were calculated to be 3.14×10^9, 1.57×10^9, 7.85×10^8, 3.92×10^8, and 1.96×10^8 particles per mL.

Table 1 reports the quantification of GNRs under different dilutions using the originally acquired OCT images and the AI-enhanced OCT images, respectively. The quantifications under different dilutions were standardized to the initial concentration by multiplying the dilution-dependent quantifications with the corresponding dilution factors. Each ROI represents one B-scan at different positions of the glass capillary tubes. We adopted 7 ROIs for each diluted solution to make more accurate quantification. In an ideal situation, the standardized particle concentrations of the diluted solutions should be identical to the particle concentration of the initial solution. The factor that the dilution changed the resulting particle concentrations indicates the interference among OCT signals of individual GNR. The signal was saturated at higher concentrations (800× dilution), resulting in a low particle concentration. Indeed, excluding the 800× dilution in analyzing the linear regression between measured and theoretical particle concentrations improved the goodness of the fit. Specifically, the R^2 metric of the fitting line was increased from 0.9584 to 0.9896 based on original OCT images, and increased from 0.9478 to 0.9940 with the AI-enhanced OCT images. Fig. 3a plots the fitting curve with the 800× dilution excluded. The linear fitting based on either the original OCT images, interpolated OCT images, or the AI-enhanced OCT images obtained close-to-one R^2, meaning the high fidelity of the linear fitting with the OCT imaging-based quantification technique. Moreover, AI-enhanced OCT images enabled further improvement of the linear fitting, indicating more accurate and more robust quantification.

Another finding from Table 1 is that with higher dilution factors, the relative standard deviation (RSD) also increases, indicating increased variations during the quantification. We

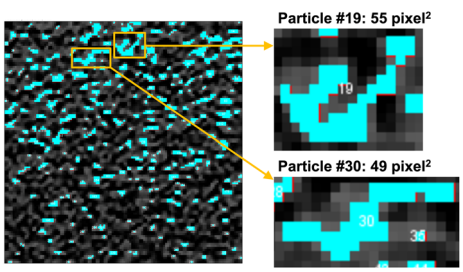

Fig. 2 Example of aggregation.

Table 1 Standardized quantification of particle concentration in the initial GNR solution. The actual quantifications in each ROI with different dilutions were standardized into the initial concentration by multiplying the corresponding dilution factors and expressed in the unit of ($\times 10^{11}$ particles per mL). "Org-OCT" and "AI-OCT" represent the originally acquired OCT images and the AI-enhanced OCT images, respectively. Values smaller than LOQ are marked with *, and values smaller than LOD are marked with **.

Dilution factor	800×		1600×		3200×		6400×		12 800×	
Method	Org-OCT	AI-OCT	Org-OCT	AI-OCT	Org-OCT	AI-OCT	Org-OCT	AI-OCT	Org-OCT	AI-OCT
ROI #1	2.328	4.655	3.550	6.391	1.578	1.894	1.578*	2.525 *	0.631**	0.631**
ROI #2	3.353	5.917	4.103	8.363	2.367	3.629	1.894	3.787	1.262*	2.525*
ROI #3	5.602	9.429	6.628	12.545	4.892	11.677	2.840	4.418	2.525	2.525*
ROI #4	6.628	10.691	9.862	15.701	7.259	14.675	2.840	7.890	5.050*	6.312
ROI #5	6.628	10.612	7.890	14.675	7.890	14.044	3.787	10.730	0.631**	1.262**
ROI #6	8.087	11.638	12.466	18.541	13.886	21.461	9.152	19.567	5.050*	8.206
ROI #7	7.772	12.111	11.914	18.226	12.782	21.776	11.36	22.407	9.468	14.518
Average	5.771	**9.293**	8.059	**13.492**	7.236	**12.737**	4.779	**10.189**	3.236	**5.140**
STD	2.182	2.888	3.549	4.687	4.772	7.799	3.863	7.915	3.218	4.962
RSD	38%	**31%**	44%	**35%**	66%	**61%**	81%	**78%**	92%	97%

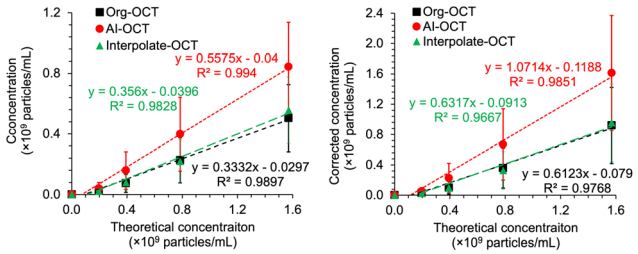

(a) No aggregation correction. (b) With aggregation correction.

Fig. 3 Correlation of OCT-based particle concentrations with theoretical concentrations and dilutions. The regression line was obtained without the 800× diluted sample. (a) No aggregation correction. (b) With aggregation correction.

assume that at low concentrations, the signal interference was too weak to make the GNRs detectable and quantifiable. Indeed, the limit of detection (LOD) and the limit of quantification (LOQ)[31] analysis showed that most ROIs of the 12 800× dilution sample had inadequate GNRs for quantification (Table 1). The high percentage of non-detectable and non-quantifiable ROIs in all the analyzed ROIs indicates reduced reliability of the particle concentration quantification. Therefore, based on Table 1, we consider the suitable dilution factors to be between 1600 and 6400, which corresponds to the particle concentration range of 4×10^8–1.6×10^9 particles per mL. This range may vary depending on the OCT signal intensity of the nanoparticles, and higher OCT signal intensity could decrease the range of the suitable particle concentration.

Within the suitable quantification range, the RSD of standardized particle concentrations of the 1600×, 3200× and 6400× dilutions is 26% and 14% based on the original and AI-enhanced OCT images, respectively. The smaller RSD provided by AI-enhanced OCT images indicates the improved robustness of quantification with the proposed AI-enhanced OCT imaging technique. The averaged particle concentration quantified with AI-enhanced OCT images was higher than those with original OCT images. While the standard deviation (STD) of the former is slightly higher, its RSD is lower. Therefore, in all the ROIs and under various dilution situations, AI-enhanced OCT imaging enabled the detection and counting of more GNRs, as well as reduced the variation among ROIs compared with results based on the original OCT images.

The OCT-based quantification results were smaller than the theoretical particle concentration, regardless of AI enhancement on OCT images. This could be due to the aggregation of GNRs in the solutions (Fig. 2). The zoom-in boxes show the detected particles with large areas, indicating substantial particle aggregations, in which case several aggregated particles were considered a single particle. To reduce the effect of aggregation in concentration quantification, we developed an algorithm to eliminate the influence of aggregation on particle concentration (see section 3).

The aggregation-corrected particle concentration of the original and AI-enhanced OCT images of the 1600× dilution was 1.43×10^{12} and 2.50×10^{12} particles per mL, respectively. Thus, the AI-enhanced OCT image provides a higher accuracy in the particle concentration quantification.

The linear fitting based on the aggregation-corrected counting is shown in Fig. 3b. The 800× dilution was not included due to signal saturation, similar to what was done for uncorrected samples. In this aggregation correction case, more GNRs were detected and counted when the concentration was high. Using AI-enhanced images provides a slightly better linear relationship between the experimental and theoretical particle concentrations compared with the original and interpolated OCT images. In Fig. 3, only the aggregation-corrected particle concentration from the AI-enhanced OCT images showed a slope of approximately 1, indicating that the resulting and theoretical particle concentrations are almost identical in the tested range. The AI-enhanced OCT image evidently offers higher accuracy in particle concentration quantification.

4 Conclusions

We have demonstrated the use of OCT imaging for the quantification of particle concentrations of nanoparticles with OCT signals, irrespective of their morphology and size distributions. GNRs were used as an illustrative example. We also developed a state-of-the-art AI-based super-resolution technique to enhance the OCT image resolution by two-fold without using any external dataset for training. We analyzed the quantification results and the linear relationship between the GNR counts and theoretical concentrations. Our results improved the quantification of nanoparticle concentration through the use of AI-enhanced OCT images compared to using conventional OCT images. In the future, we will investigate the performance of the proposed method in other diluent media or tissues.

Conflicts of interest

There are no conflicts to declare.

Acknowledgements

We acknowledge the support of Prof. Jeffrey L. Goldberg. This work was supported by the National Eye Institute (K99EY034168 and P30EY026877), National Cancer Institute (R01CA227713 and R01CA256890), and a departmental core grant from Research to Prevent Blindness, Inc.

References

1 J. R. Cook, W. Frey and S. Emelianov, *ACS Nano*, 2013, **7**, 1272–1280.
2 S. Mallidi, T. Larson, J. Tam, P. P. Joshi, A. Karpiouk, K. Sokolov and S. Emelianov, *Nano Lett.*, 2009, **9**, 2825–2831.
3 A. de la Zerda, S. Prabhulkar, V. L. Perez, M. Ruggeri, A. S. Paranjape, F. Habte, S. S. Gambhir and R. M. Awdeh, *Clin. Exp. Ophthalmol.*, 2015, 358–366.
4 F. Chen, P. Si, A. De La Zerda, J. V. Jokerst and D. Myung, *Biomater. Sci.*, 2021, **9**, 367.
5 J. Hu, F. Rivero, R. A. Torres, H. Loro Ramírez, E. M. Rodríguez, F. Alfonso, J. García Solé and D. Jaque, *J. Biophotonics*, 2017, **10**, 674–682.
6 C. S. Kim, P. Wilder-Smith, Y. C. Ahn, L. H. L. Liaw, Z. Chen and Y. J. Kwon, *J. Biomed. Opt.*, 2009, **14**(3), 034008.
7 R. Meir, K. Shamalov, O. Betzer, M. Motiei, M. Horovitz-Fried, R. Yehuda, A. Popovtzer, R. Popovtzer and C. J. Cohen, *ACS Nano*, 2015, **9**, 6363–6372.
8 T. Nakagawa, K. Gonda, T. Kamei, L. Cong, Y. Hamada, N. Kitamura, H. Tada, T. Ishida, T. Aimiya, N. Furusawa, Y. Nakano and N. Ohuchi, *Sci. Technol. Adv. Mater.*, 2016, **17**, 387–397.
9 C. Peng, L. Zheng, Q. Chen, M. Shen, R. Guo, H. Wang, X. Cao, G. Zhang and X. Shi, *Biomaterials*, 2012, **33**, 1107–1119.
10 H. S. Kim and D. Y. Lee, *Polymers*, 2018, **10**, 961.
11 J. Lin, S. Wang, P. Huang, Z. Wang, S. Chen, G. Niu, W. Li, J. He, D. Cui, G. Lu, X. Chen and Z. Nie, *ACS Nano*, 2013, **7**, 5320–5329.
12 A. Gharatape, S. Davaran, R. Salehi and H. Hamishehkar, *RSC Adv.*, 2016, **6**, 111482–111516.
13 H. Norouzi, K. Khoshgard and F. Akbarzadeh, *Lasers Med. Sci.*, 2018, **33**, 917–926.
14 J. B. Vines, J. H. Yoon, N. E. Ryu, D. J. Lim and H. Park, *Front. Chem.*, 2019, **7**, 432792.
15 G. Ajnai, A. Chiu, T. Kan, C. C. Cheng, T. H. Tsai and J. Chang, *J. Exp. Clin. Med.*, 2014, **6**, 172–178.
16 Y. Chen and X. Feng, *Int. J. Pharm.*, 2022, **625**, 122122.
17 T. K. Hornsby, F. M. Kashkooli, A. Jakhmola, M. C. Kolios and J. Tavakkoli, *Cancers*, 2023, **15**, 523.
18 C. Zhou, A. B. Krueger, J. G. Barnard, W. Qi and J. F. Carpenter, *J. Pharm. Sci.*, 2015, **104**, 2441–2450.
19 W. Oosthuyzen, N. E. L. Sime, J. R. Ivy, E. J. Turtle, J. M. Street, J. Pound, L. E. Bath, D. J. Webb, C. D. Gregory, M. A. Bailey and J. W. Dear, *J. Physiol.*, 2013, **591**, 5833–5842.
20 N. T. Le, T. J. M. Boskovic, M. M. Allard, K. E. Nick, S. R. Kwon and C. C. Perry, *ACS Omega*, 2022, **7**, 44677–44688.
21 P. Singh, J. Bodycomb, B. Travers, K. Tatarkiewicz, S. Travers, G. R. Matyas and Z. Beck, *Int. J. Pharm.*, 2019, **566**, 680–686.
22 N. Hondow, R. Brydson and A. Brown, *J. Phys.: Conf. Ser.*, 2014, **522**, 012055.
23 W. H. De Jong, M. C. Burger, M. A. Verheijen and R. E. Geertsma, *Materials*, 2010, **3**, 4681–4694.
24 C. Mühlfeld, B. Rothen-Rutishauser, D. Vanhecke, F. Blank, P. Gehr and M. Ochs, *Part. Fibre Toxicol*, 2007, **4**, 1–17.
25 R. Allabashi, W. Stach, A. De La Escosura-Muñiz, L. Liste-Calleja and A. Merkoçi, *J. Nanopart. Res.*, 2009, **11**, 2003–2011.
26 Y. Jia, G. Liu, A. Y. Gordon, S. S. Gao, A. D. Pechauer, J. Stoddard, T. J. McGill, A. Jayagopal and D. Huang, *Opt. Express*, 2015, **23**, 4212–4225.
27 P. Si, S. Shevidi, E. Yuan, K. Yuan, Z. Lautman, S. S. Jeffrey, G. W. Sledge and A. de la Zerda, *Nano Lett.*, 2019, **20**, 101–108.
28 S. Ye, L. Shen, M. T. Islam and L. Xing, *Phys. Med. Biol.*, 2023, **68**, 205020.
29 ImageJ, **https://imagej.net/ij/index.html**.
30 M. A. Mackey, M. R. Ali, L. A. Austin, R. D. Near and M. A. El-Sayed, *J. Phys. Chem. B*, 2014, **118**, 1319–1326.
31 A. Shrivastava, V. B. Gupta, *et al.*, *Chron. Young Sci.*, 2011, **2**, 21–25.

